Chapter 10
Zirconia

Olivia A. Graeve

Abstract Zirconia is a very important industrial ceramic for structural applications because of its high toughness, which has proven to be superior to other ceramics. In addition, it has applications making use of its high ionic conductivity. The thermodynamically stable, room temperature form of zirconia is baddeleyite. However, this mineral is not used for the great majority of industrial applications of zirconia. The intermediate-temperature phase of zirconia, which has a tetragonal structure, can be stabilized at room temperature by the addition of modest amounts (below ~8 mol%) of dopants such as Y^{3+} and Ca^{2+}. This doped zirconia has mechanical toughness values as high as 17 MPa•$m^{1/2}$. On the other hand, the high-temperature phase of zirconia, which has a cubic structure, can be stabilized at room temperature by the addition of significant amounts (above ~8 mol%) of dopants. This form of zirconia has one of the highest ionic conductivity values associated with ceramics, allowing the use of the material in oxygen sensors and solid-oxide fuel cells. Research on this material actively continues and many improvements can be expected in the years to come.

1 Introduction

Zirconia (ZrO_2) is an extremely versatile ceramic that has found use in oxygen pumps and sensors, fuel cells, thermal barrier coatings, and other high-temperature applications, all of which make use of the electrical, thermal, and mechanical properties of this material. Proof of the interest and usefulness of zirconia can be seen from the voluminous literature found on this material. This chapter is intended to provide a concise summary of the physical and chemical properties of all phases of zirconia that underlie the appropriate engineering applications.

The three low-pressure phases of zirconia are the monoclinic, tetragonal, and cubic, which are stable at increasingly higher temperatures. Calculated energy vs. volume data at zero absolute temperature confirms the higher stability of the monoclinic phase (Fig. 1). However, most engineering applications make use of the tetragonal and cubic phases, even though their stability at low temperatures is quite low. In fact, the engineering use of all three phases of zirconia in pure form is rare. Generally,

J.F. Shackelford and R.H. Doremus (eds.), *Ceramic and Glass Materials: Structure, Properties and Processing*.

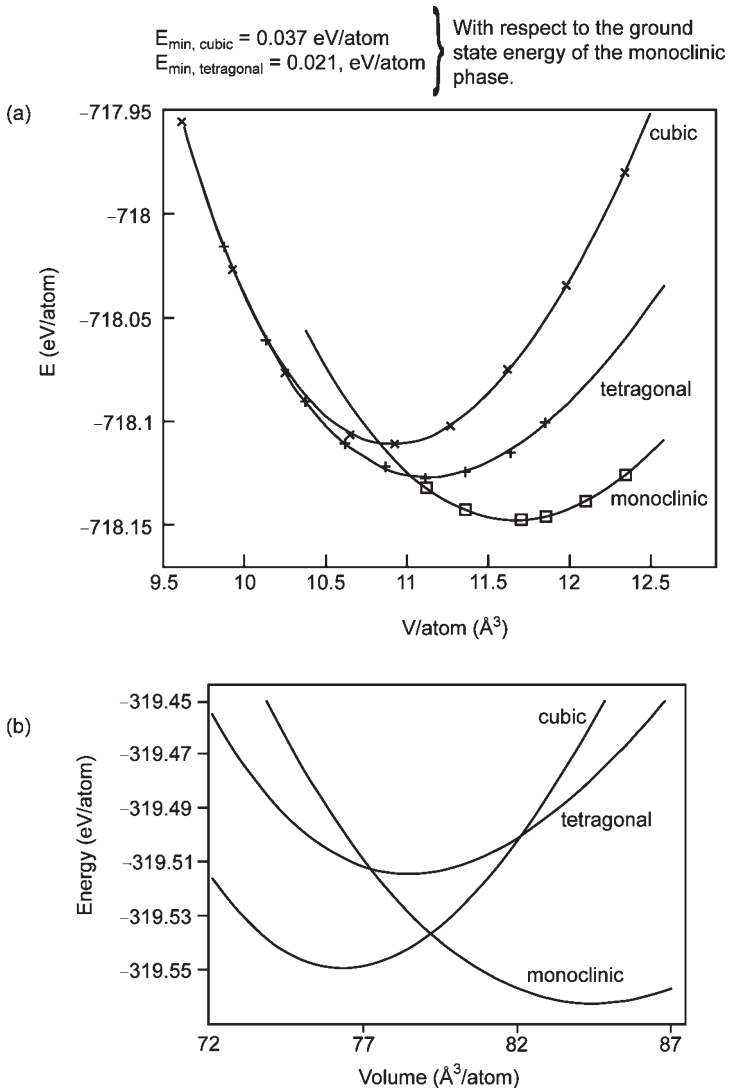

Fig. 1 Computed energy vs. volume data for cubic, tetragonal, and monoclinic phases from (**a**) Stapper et al. [1] and (**b**) Dewhurst and Lowther [2] (reprinted with permission)

zirconia is doped with oxides such as Y_2O_3 that stabilize the high-temperature phases at room temperature. This has enormous consequences for both the mechanical and electrical properties of zirconia, even though the local atomic and electronic structure of Zr^{4+} in all three polymorphs is for the most part dopant independent [3].

Doping of zirconia results in stabilization of the tetragonal phase at lower dopant concentrations (for mechanical toughness) or the cubic phase at higher dopant concentrations (for high ionic conductivity) at room temperature. The stabilization of the tetragonal phase at room temperature can result in the following common forms of

zirconia: (1) partially stabilized zirconia (PSZ) – zirconia consisting of a matrix of a brittle ceramic and a dispersion of tetragonal precipitates, where the tetragonal precipitates can either be in pure form or doped with Ca^{2+} (Ca-PSZ) or Mg^{2+} (Mg-PSZ); and (2) tetragonal zirconia polycrystals (TZP) – zirconia consisting of a matrix of stabilized ZrO_2 that has been stabilized in the tetragonal form by the addition of dopants such as Ce^{4+} (Ce-TZP) and Y^{3+} (Y-TZP). Fully-stabilized zirconia (FSZ) refers to a material that has been completely stabilized in the cubic form.

Stabilized zirconia in thermal barrier coatings (TCB) is ubiquitous, finding itself in combustor liners, transition sections, nozzle guide vanes, and rotor blades. It is one of the most used ceramics for TCB applications because of its low thermal conductivity, high-temperature stability in oxidizing and reducing environments, coefficient of thermal expansion similar to iron alloys, high toughness, and cost-effectiveness by which it can be applied onto metal surfaces. Its use allows a 200°C increase in the operational temperature of the engine, resulting in a much higher efficiency [4].

The second, well-known use of stabilized zirconia is in oxygen sensors. These types of devices make use of the very high ionic conductivity of Y_2O_3- or CaO-doped cubic zirconia. The sensor assembly consists of a zirconia tube with one end closed. The inside of this tube is exposed to air and the outside is exposed to the gas that requires measurement of oxygen levels. When there is a difference in oxygen partial pressure between the inside and outside, oxygen is transported across the ceramic tube. This transport results in a measurable voltage.

A solid-oxide fuel cell (SOFC) functions similar to an oxygen sensor. An SOFC converts the chemical energy of a fuel directly to electrical energy and heat and consists of two electrodes that sandwich an electrolyte, allowing ions to pass while blocking electrons. The air electrode allows oxygen to pass through to the electrolyte. At the electrolyte interface, the oxygen dissociates into ions that travel across the electrolyte via ionic conduction. Typical SOFC's consist of an Y_2O_3-doped ZrO_2, with about 8 mol% yttrium, as the electrolyte. At the fuel electrode, the oxygen ions that have traveled across the electrolyte react with the fuel forming H_2O and possibly other gases, depending on the type of fuel used. During the reaction, at the fuel electrode/electrolyte interface, electrons are generated that travel through an external circuit, thus generating electrical current that can be used for doing external work. This technology will become increasingly important as a "clean" source of electricity as pressures on the environment from the use of coal and petroleum continue to increase.

2 Crystalline and Noncrystalline Structures

The complex crystallography of zirconia plays an important role in the challenges to develop commercially viable applications of this material. At room temperature, bonding in this material is a combination of ionic and covalent and results in a structure in which zirconium is seven-coordinated, which is rather unusual and is a product of the large difference in ionic sizes between zirconium and oxygen. The formation of this material from pure α-Zr and oxygen starts at around 23 at.% O, corresponding to a composition of $ZrO_{0.3}$ [5]. The perfect stoichiometry for this material in which there is one zirconium and two oxygen ions for each formula unit is not used in industrial applications. Doping of the structure produces oxygen vacancies resulting

in chemical formulas of the type $ZrCa_xO_{2-x}$, for the case of CaO doping, to maintain charge balance in the structure.

2.1 Cubic Zirconia

Cubic zirconia (Fm3m) has a fluorite structure with one formula unit ($Z = 1$) in the primitive cell. This cell contains one zirconium ion located at (0, 0, 0) and coordinated with eight equidistant oxygen ions. The two oxygen ions are located at (¼, ¼, ¼) and (¾, ¾, ¾), both tetrahedrally coordinated to four zirconium ions. The nonprimitive face-centered arrangement is illustrated in Fig. 2 and contains four zirconium ions located at (0, 0, 0), (½, ½, 0), (½, 0, ½), and (0, ½, ½). The eight oxygen ions are located at (¼, ¼, ¼), (¼,¼, ¾), (¼, ¾, ¼), (¾, ¼, ¼), (¾, ¾, ¼), (¾, ¼, ¾), (¼, ¾, ¾), and (¾, ¾, ¾). The translational vectors for this structure are

$$\begin{aligned} t_1 &= \left(0, \tfrac{a}{2}, \tfrac{a}{2}\right), \\ t_2 &= \left(\tfrac{a}{2}, 0, \tfrac{a}{2}\right), \\ t_3 &= \left(\tfrac{a}{2}, \tfrac{a}{2}, 0\right). \end{aligned} \tag{1}$$

General crystallographic correlations for this structure are given in Table 1. Experimental measurements of the lattice parameter, a_c, at 2,683, 2,388, and 2,503 K result in 0.5269, 0.52438, and 0.5247 nm, respectively. The measurement at 2,683 K was done

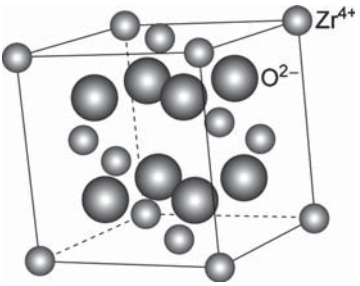

Fig. 2 Crystal structure of cubic zirconia as seen from the [153] direction

Table 1 General crystallographic correlations in cubic zirconia

Space group	Fm3m
Reflection conditions	*hkl*: $h + k$, $k + l$, $l + h = 2n$ 0*kl*: k, $l = 2n$ *hhl*: $h + l = 2n$ *h*00: $h = 2$
Coordination number	8
Z	1
Lattice parameter	a_c
Unit cell volume	$V_c = a_c^3$
Ionic positions	Zr^{4+}: 4a O^{2-}: 8c

in a neutral atmosphere, while the latter two measurements were done in a reducing atmosphere [6]. At increasing pressures, the lattice parameter changes to 0.4947, 0.4925, and 0.4916 nm for pressures of 28.9, 33.8, and 37.3 GPa, respectively [7].

2.2 Tetragonal Zirconia

The tetragonal zirconia structure (Fig. 3 [6], Table 2), with space group $P4_2/nmc$ (primitive) [8, 9] and a cation coordination number of 8, is derived from the cubic fluorite structure by the movement of oxygen anions along one of the cubic axes, which results in a tetragonal distortion along that axis, as shown in Fig. 3 for a distortion along the *c*-axis. The two zirconium ions in the primitive structure are located at (0, 0, 0) and (½, ½, ½), and the four oxygen ions are located at (0, ½, *z*), (½, 0, −*z*), (0, ½, ½ + *z*), and (½, 0, ½ −*z*), where $z = 0.185$. This results in a body-centered tetragonal (bct) structure, which is sometimes described as a pseudofluorite structure.

The transition from cubic to tetragonal is displacive in which four Zr^{4+} cations in the 4a cubic positions split into two groups to occupy the 2b positions in the tetragonal structure, and the O^{2-} anions in the 8c cubic positions also split into two groups to occupy the 4d positions in the tetragonal structure. The directions of *a* and *b* axes in the tetragonal primitive lattice are 45° from those in the cubic cell. The *c* axis in both structures remains the same. Following the literature convention of reporting the parameter $d_z = 0.25 - z$, where *z* represents the third coordinate of the oxygen position 4d (0, ½, *z*), the calculated *c*/*a* ratio and internal parameter d_z of the tetragonal phase as a function of volume are shown in Fig. 4 [2].

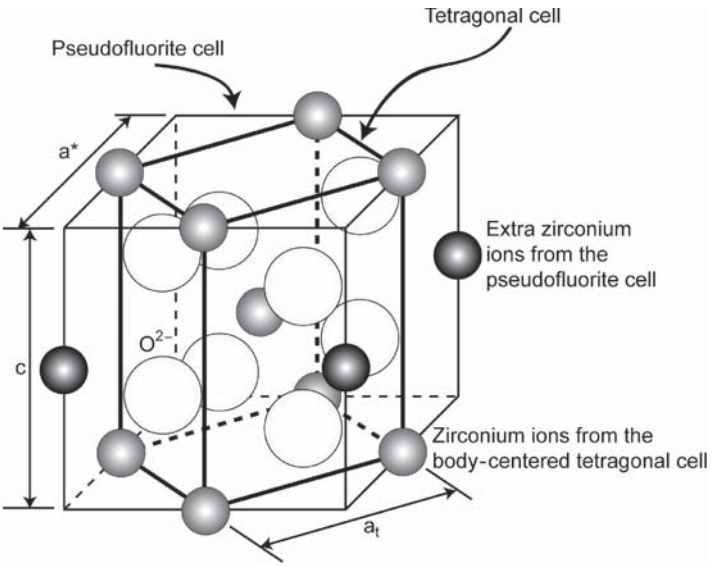

Fig. 3 Tetragonal zirconia unit cell in both the body-centered tetragonal and pseudofluorite descriptions (adapted from Aldebert and Traverse [6])

Table 2 General crystallographic correlations in tetragonal zirconia

Space group	$P4_2/nmc$
Reflection conditions	$hk0$: $h + k = 2n$
	hhl: $l = 2n$
	$00l$: $l = 2n$
	$h00$: $h = 2n$
Coordination number	8
Z	2
Lattice parameters	$a_t = b_t \approx a^*/\sqrt{2}$
	$c_t \approx a^*$
Unit cell volume	$V_t \approx V_c/2$
Ionic positions	Zr^{4+}: 2b
	O^{2-}: 4d

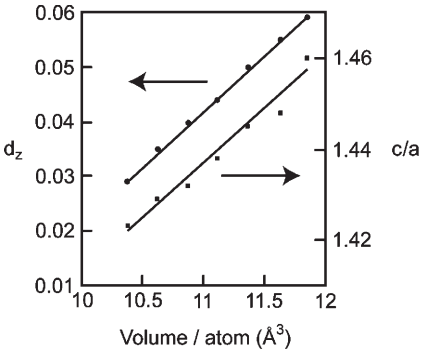

Fig. 4 Calculated *c*/*a* ratio and internal structural parameter, d_z, of the tetragonal phase as a function of volume [2] (reprinted with permission)

2.3 Monoclinic Zirconia

EXAFS analysis by Winterer [10] and Li et al. [11] shows that monoclinic ZrO_2 can be described by a sevenfold Zr–O shell with an average distance of 0.216 nm and a mean vibrational frequency of 410 cm^{-1}. The structure consists of layers of triangular coordination polyhedra of three O_1–Zr bonds and four distorted tetrahedral O_2–Zr bonds for a total of seven oxygen ions surrounding the zirconium [10], as shown in Fig. 5. In this illustration, there are three unit cells that help with visualization. The Zr^{4+} sublattice is marked with dashed lines and the seven coordinating oxygen ions surrounding the darker-colored zirconium ion are marked with numbers. The plane that constitutes the O_1 atoms is nearly parallel to the plane of O_2 atoms. The general crystallographic correlations for this structure are listed in Table 3. The Zr–O distances range from 0.1885 to 0.2360 nm for the O_1–Zr shell and 0.1914 to 0.2511 nm for the O_2–Zr shell.

There are also three distinct Zr–Zr subshells at 0.346,[1] 0.396 (0.401),[2] and 0.454 (0.455) nm with a total of 12 zirconium next nearest neighbors at an average distance of 0.372 nm. The coordination numbers for the first, second, and third subshells of the

[1] Winterer and Li *et al*. report the same value.

[2] First value by Winterer; value in parentheses by Li et al.

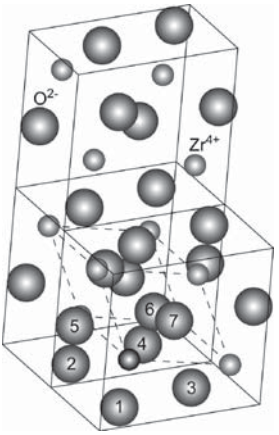

Fig. 5 Crystal structure of monoclinic zirconia as seen from the $[1\bar{3}1]$ direction

Table 3 General crystallographic correlations in monoclinic zirconia

Space group	$P2_1/c$
Reflection conditions	$h0l$: $h + l = 2n$
	$0k0$: $k = 2n$
	$h00$: $h = 2n$
	$00l$: $l = 2n$
Coordination number	7
Z	4
Lattice parameters	$a_m \neq b_m \approx a_c$
	$c_m > a_c$
Unit cell volume	$V_m \approx 2V_c$
Ionic positions	Zr^{4+}: 4e
	O_I^{2-}: 4e
	O_{II}^{2-}: 4e

Zr–Zr bonds are 7, 4, and 1, respectively. The zirconium ions form layers parallel to the (100) planes of the unit cell, with the O_1 ions on one side and the O_2 ions on the other side. The distance between two layers of zirconium ions is larger when they are separated by O_1 ions.

2.4 High-Pressure Phases

High-pressure experimental measurements on ZrO_2 have revealed that the ambient monoclinic baddeleyite phase transforms under increasingly higher pressures to a series of orthorhombic phases. The first orthorhombic phase starts appearing at an applied pressure of about 3.5 GPa [13], depending upon the crystallite size of the material – lower crystallite size results in a higher transformation pressure [14], although the phase transformation is not completed until 10 ± 1 GPa, as determined by Desgreniers and Lagarec [15]. The calculated (ab initio) transition pressure, according to Stapper et al. [2], is 5.7 GPa, so experimental measurements and ab initio

calculations are in general agreement. This first orthorhombic phase (Pbca [16], $Z = 8$, coordination number = 7) is observed to exist up to about 25 GPa when a second orthorhombic structure appears (Pnma, $Z = 4$, coordination number = 9), although the precise onset pressure has not been determined accurately. This phase is stable at ambient temperature up to at least 70 GPa. A projection of the crystal structure is illustrated in Fig. 6 [17]. The change in volume with pressure is shown in Fig. 7 [15], where the initial volume, V_o, is taken as 70.32 Å.

Aside from the two high-pressure phases of zirconia, a hexagonal high-temperature and high-pressure phase was found by Ohtaka et al. [18] by quenching pure ZrO_2 powders from above 1,000°C and 20 GPa. This hexagonal structure ($Z = 8$) reverts to the baddeleyite structure when pressure is released below 1 GPa.

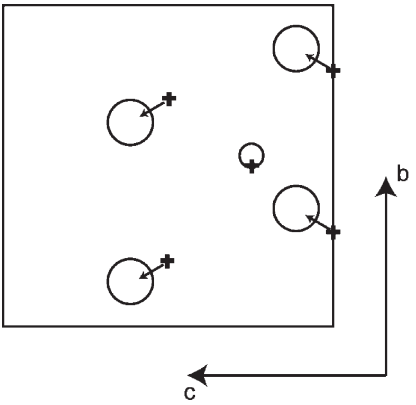

Fig. 6 A projection into (100) of the orthorhombic-I structure. The *crosses* indicate the atom positions in the tetragonal structure, and the *arrows* the presumed displacements of these atoms during the transition to orthorhombic [17] (reprinted with permission)

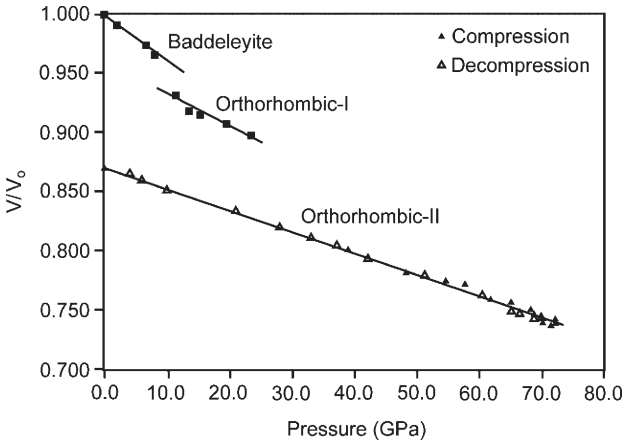

Fig. 7 Pressure dependence of the volume of the dense phases of zirconia [15] (reprinted with permission)

2.5 Amorphous Structure

When ZrO_2 powders are prepared using any number of precipitation methodologies, the resulting structure before calcination is amorphous [19–22]. Detailed studies by Chadwick et al. [23] have shown that the amorphous gel has both OZr_3 and OZr_4 environments in approximately equal proportions, as evidenced from the two ^{17}O NMR peaks at 405 ppm and 303 ppm, respectively. EXAFS results show that there is a well-defined oxygen shell with a coordination number of 7 at ~0.214 nm and a second shell with a much smaller coordination number at ~0.342 nm corresponding to the Zr–Zr correlation. The NMR and Zr K-edge EXAFS results unambiguously indicate that the short-range structure of the amorphous gel is monoclinic-like.

Once the amorphous gel is heated, ^{17}O NMR shows that both OZr_3 and OZr_4 environments remain, although there is an increase in line width. There is also an increase in the isotropic chemical shift of the peaks, especially the OZr_4 peak, which moves from 303 to 321 ppm as the gel starts to crystallize. At the crystallization temperature (approximately 360°C), EXAFS results show that there is a distinct change in the structure, with the oxygen correlation now better fit by two closely spaced shells and a large increase in the coordination number to 12 associated with the Zr–Zr correlation. This is likely because the particles are nanocrystalline.

After crystallization has occurred, there is an additional ^{17}O NMR peak at 374 ppm that corresponds to OZr_4 in tetragonal ZrO_2. However, the NMR data show that although crystalline tetragonal ZrO_2 is forming at the point of crystallization, oxygen is still present as part of the disordered ZrO_2. Upon further heating, the tetragonal content increases significantly, but at no time is there complete elimination of the disordered ZrO_2.

In addition, ^1H NMR results show that, even after crystallization, it is not correct to describe the sample composition as ZrO_2. Data show that, after being heated to 300°C, the sample's composition is $ZrO_{1.42}(OH)_{1.16}$. At 500°C, well above the crystallization temperature, it is still $ZrO_{1.76}(OH)_{0.48}$. The OH^- content found below this temperature is not related to the usual surface hydroxylation upon exposure to the atmosphere, instead the hydroxyls are structural units within the sample. Above 700°C, the hydroxide content is no longer measurable and with subsequent heating the sample changes to the monoclinic structure. Hence, the reaction for the formation of zirconia by precipitation can be described as:

$$Zr_4O_{(8-x)}(OH)_{2x} \rightarrow ZrO_{(2-y/2)}(OH)^y(amorphous) \rightarrow$$
$$ZrO_{(2-z/2)}(OH)_z(tetragonal, crystalline; monoclinic-like, disordered) \rightarrow$$
$$ZrO_2(monoclinic, crystalline)$$

There is an initial metal hydroxide that becomes an amorphous oxide containing hydroxyls. With heating, some of these hydroxyls are lost, resulting in the formation of a mixture with more-ordered tetragonal and less-ordered monoclinic components. With further heating, the eventual crystalline product becomes monoclinic.

In contrast, an EXAFS analysis from amorphous zirconia films of nominal ZrO_2 composition, as opposed to a hydroxide composition, found that the local structure in amorphous ZrO_2 can be described by an eightfold Zr–O shell widely spread between 0.19 and 0.32 nm with a distinct peak at 0.216 nm consisting of four oxygen nearest

neighbors. The average Zr–O coordination distance is 0.255 nm for all eight oxygen neighbors. The local structure also consists of a very broad Zr–Zr shell at about 0.41 nm with 12 next nearest neighbors [10].

3 Point Defects

Point defects play a central role in the use of zirconia ceramics in such applications as oxygen sensors and fuel cells. As a result, point defects in these materials have been extensively studied.

3.1 Interstitial Defects

Interstitial defects in monoclinic zirconia have been modeled in detail by Foster et al. [24]. Using plane wave density functional theory, the tetragonal bonding and triple-planar bonding geometries of lattice oxygen ions were determined. In addition, it was determined that interstitial defects can form stable defect pairs with either type of lattice oxygen ions (i.e., tetragonal or triply bonded). The analysis looked at defect pairs formed by interstitial oxygen ions with three possible charge states: 0, −1, and −2, bonded to triple-planar lattice oxygen ions. An analysis of oxygen vacancies both in the triple-planar and tetragonal geometries was also undertaken.

A neutral oxygen interstitial forming a defect pair with a triple-bonded oxygen is illustrated in Fig. 8 [24]. Using the oxygen atomic energy as a reference, a single neutral oxygen can be incorporated in the lattice as an interstitial with an energy gain of −1.6 eV, if next to a triple-bonded lattice oxygen, and −0.8 eV, if next to a tetragonally bonded lattice oxygen. Figure 8 illustrates the fully relaxed charge density and positions of ions, showing that the interstitial and lattice oxygen form a strong covalent bond. The labels A and B associated with the lattice ions represent two different crystal planes within the structure. The lattice oxygen (O_A), forming the defect pair with the interstitial oxygen, relaxes by up to 0.05 nm to accommodate the interstitial, distorting the triply-bonded oxygen with respect to the three zirconium ions bonded to it. The O–3Zr group has a slight pyramidal shape with its apex pointing away from the interstitial. The rest of the crystal remains more or less undisturbed, with the nearest zirconium (Zr_A) only relaxing by about 0.005 nm. The case of a singly-charged oxygen interstitial forming a defect pair with a triply-bonded oxygen results in weakening of the covalent bond between the defect pair significantly. The extreme is the case of a doubly-charged oxygen interstitial in which the interstitial forms elongated bonds with the zirconium ions and occupies a new triple site, which is bonding with the Zr_A, Zr_B, and a new zirconium ion.

3.2 Vacancy Defects

Oxygen vacancies in cubic zirconia result in a calculated displacement pattern as shown in Fig. 9 [2]. In this figure, the vacancy is depicted as a small cube, the oxygen

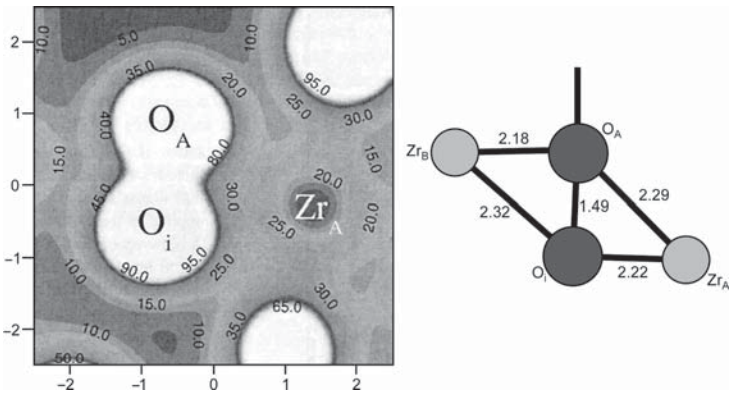

Fig. 8 Charge density in the plane through Zr_A, O_A, and O_i, and a schematic diagram of a neutral oxygen interstitial (O_i) near a triple-bonded oxygen (O_A) in zirconia. Charge density is in 0.1 eV Å^{-1} and all distances are in Å [24] (reprinted with permission)

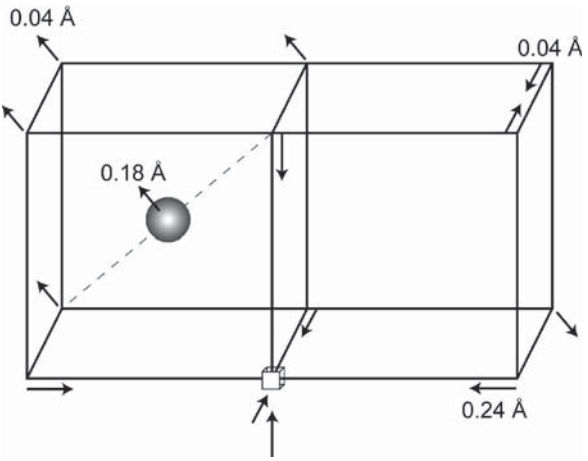

Fig. 9 Displacement pattern of atoms around an isolated vacancy in a 95 atom supercell [2] (reprinted with permission)

atoms occupy the sites at the corners of the cubes, and metal cations occupy half of the sites at the center of the cubes. The six oxygen neighbors nearest to the vacancy move along <100> by 0.024 nm, while the zirconium atoms move outward along <111> by 0.018 nm. The oxygen atoms nearest to the zirconium, but not nearest to the vacancy, follow the displacement of the cation and move outwards along <111> by 0.004 nm. The oxygen atoms in the outermost right corner of the figure move inwards by 0.004 nm along <111>.

Tetragonal zirconia contains anion vacancies and may be written as ZrO_{2-x}, with x varying from 0.001 at 1,925°C to 0.052 at 2,410°C [6]. To accommodate these vacancies, surrounding ions move toward the vacancy to reduce its size. The two zirconium ions move by an approximate amount of 0.008 nm and the oxygen ions by 0.013 nm. The energy gain due to the relaxation of these ions is 0.22 eV. These values are, of course, different depending on the charge of the vacancy [25].

For the case of a singly-charged vacancy, the structural distortion results in the movement of surrounding oxygen ions by an approximate amount of 0.022 nm toward the vacancy and the zirconium ions by 0.009 nm away from the vacancy. These values are modified for the case of a doubly-charged vacancy to 0.033 nm for the oxygen ions and 0.022 nm for the zirconium ions. Obviously, the higher the positive charge of the vacancy, the greater the distortion towards or away from it. The energy gains due to the formation of singly- and doubly-charged vacancies are 1.0 and 3.3 eV, respectively.

Oxygen vacancies in monoclinic zirconia can occur in both the triple-planar and tetragonal geometries. When the vacancy is neutral, these vacancies have formation energies of 8.88 eV and 8.90 eV, respectively. Once the vacancy is singly charged positively (i.e., V^{+}) and in a tetrahedral position, the atomic relaxation energy is 0.47 eV. Creation of a doubly-charged positive vacancy (i.e., V^{2+}) in a tetrahedral position causes further displacement of the four surrounding zirconium ions away from the vacancy by an additional 0.01 nm. This leads to a further decrease in energy of 0.74 eV. Creation of a singly-charged negative vacancy (i.e., V^{-}) in the same tetrahedral position causes minimal displacement of the surrounding zirconium ions (by less than 0.002 nm) and an energy decrease that is less than 0.1 eV, which clearly points to the fact that the additional electron is only weakly localized in the vicinity of the vacancy and, hence, has little influence on the surrounding ions. The lattice relaxation and formation energies in the case of a neutral zirconium vacancy are about 1.4 and 24.2 eV, respectively. The oxygen ions surrounding this type of vacancy are displaced outwards from their equilibrium positions by about 0.01–0.02 nm.

At higher temperatures (i.e., 1,000°C) and excess partial pressure of oxygen (i.e., 10^{-6} to 1 atm.), monoclinic zirconia contains completely ionized zirconium vacancies [26]. At 1,000°C, zirconia is stoichiometric at a pressure of 10^{-16} atm. At this point, the concentration of oxygen vacancies is equal to twice the concentration of zirconium vacancies. As the partial pressure of oxygen increases, the stoichiometry changes such that for $ZrO_{2+\delta}$, with the δ value defined by:

$$\delta = 6 \times 10^{-3}\ p_{O_2}^{1/5}, \tag{2}$$

where po_2 is the oxygen partial pressure in atm.

4 Mechanical Properties

Measurements of the mechanical properties of pure tetragonal and cubic zirconia are exceedingly difficult because of the higher temperatures required for such measurements. Hence, only monoclinic zirconia has been thoroughly studied in pure form. The mechanical properties of tetragonal and cubic zirconia have been determined for many stabilized zirconias and, because of the importance of these materials in engineering applications, several reviews have been written [27–29].

4.1 Elastic Properties

The measured elastic stiffness and compliance moduli for monoclinic zirconia have been summarized by Chan et al. [30]. The Young's and shear moduli of this same

Table 4 Polycrystalline Young's and shear moduli for monoclinic zirconia in GPa (adapted from Chan et al. [30]

	20°C	300°C	600°C	800°C	1,000°C
E_{Voigt}	266	256	250	245	239
E_{Reuss}	215	216	220	222	214
E_{Hill}	241	236	235	234	226
G_{Voigt}	104	99.1	96.8	94.9	92.6
G_{Reuss}	83.4	83.2	84.7	85.3	82.4
G_{Hill}	93.6	91.1	90.7	90.1	87.5

structure are given in Table 4 and were calculated using the Voigt, Reuss, and Hill approximations. The Voigt and Reuss approximations usually give the upper and lower bounds of these parameters. The maximum errors in these numbers are about 10% for most values, but can increase to greater than 20% for some of the transverse directions in the crystal.

For the monoclinic and tetragonal structures, the bulk modulus hovers around 150–200 GPa. Cubic zirconia has higher bulk modulus somewhere around 171–288 GPa. The high-pressure phases have values around 224–273 GPa and 254–444 GPa, for the orthorhombic-I and orthorhombic-II phases, respectively.

4.2 Hardness

The hardness for monoclinic zirconia is approximately 9.2 GPa [31] for samples with a density >98% and 4.1–5.2 GPa [32] for samples with a density >95% of theoretical, whereas hardness values for amorphous zirconia vary between 5 and 25 GPa [33]. The hardness increases slightly to values approaching 11 GPa for yttria-stabilized zirconia of 1.5 mol% yttria, which is stabilized in the tetragonal form [31]. Addition of larger amounts of yttria dopant results in hardness values approaching 15 GPa [34].

4.3 Toughness

The toughness of pure monoclinic zirconia is difficult to obtain because of problems encountered during sintering of these types of specimens. Generally, if a full density is desired for mechanical properties evaluation, the material needs to be heated to a temperature that is above the tetragonal-to-monoclinic transformation temperature (i.e., 1,471 K). This results in severe cracking upon cooling. However, there have been a few studies that have shown that nanocrystalline monoclinic zirconia can be sintered to full density at 1,273 K. In this case, microcracking during cooling can be avoided [35]. Unfortunately, these specimens have not been tested for toughness.

Experiments have been attempted with porous specimens of monoclinic zirconia and the fracture toughness has been extrapolated. A value of 2.06 ± 0.04 MPa $m^{1/2}$ was found for a specimen of 92.2 ± 0.4 % relative density, from which a fracture toughness

of 2.6 MPa $m^{1/2}$ was extrapolated for a specimen of full density [36]. Slightly higher numbers of 3.7 ± 0.3 MPa•$m^{1/2}$ were found for specimens with >95% density [32]. Evidently, the fracture toughness of this phase of zirconia is quite low. The toughness of cubic zirconia is also low, reported as 2.8 MPa $m^{1/2}$ by Chiang et al. [37] and 1.8 ± 0.2 MPa•$m^{1/2}$ by Cutler et al. [32].

The addition of alloying elements such as Y^{3+}, Ce^{3+}, and Mg^{2+} can result in stabilization of tetragonal zirconia, which results in an increase in the fracture toughness of the material via a process of transformation toughening. The addition of increasing amounts of the stabilizing elements results in the stabilization of the cubic phase, which does not have transformation-toughening behavior. Toughening requires the presence of the metastable tetragonal phase.

As can be seen in Fig. 10 [29], the fracture toughness in polycrystalline tetragonal zirconia (TZP) and partially-stabilized zirconia (PSZ) appears to reach a maximum. This indicates a transition from flaw-size control of strength to transformation-limited strength. Ranges of fracture toughness values for zirconia composites are given by Richerson [38].

The stability of the tetragonal structure can be controlled by three factors: the grain size [39, 40], the constraint from a surrounding matrix [41, 42], and the amount of dopant additions. Commonly, very small tetragonal particles are added as a reinforcing phase to a matrix of another material, which is usually brittle (i.e., pure cubic or monoclinic zirconia, alumina [43], Si_3N_4 [44], and others [45]) as shown in Fig. 11a. This results in a higher overall toughness for the composite. For example, Gupta et al. [46] has shown that the addition of small tetragonal particles to a matrix of monoclinic zirconia results in an increment of the toughness to values between 6.07 and 9.07 MPa•$m^{1/2}$, in contrast to the low numbers observed for pure monoclinic zirconia. A review on the transformation toughnening of several zirconia composites has been prepared by Bocanegra-Bernal and Diaz De La Torre [42].

This toughening mechanism is associated with the increase in volume upon transformation to the monoclinic phase. Since the monoclinic phase occupies a larger volume compared with the tetragonal phase, it forces closure of any propagating cracks, greatly diminishing the catastrophic failure of the material due to fracture [47]. In addition, the transformation from tetragonal to monoclinic results in energy absorption that blunts the crack.

The transformation is induced by an applied stress on the material. Initially, a ceramic composite may contain a crack that begins to propagate upon application of

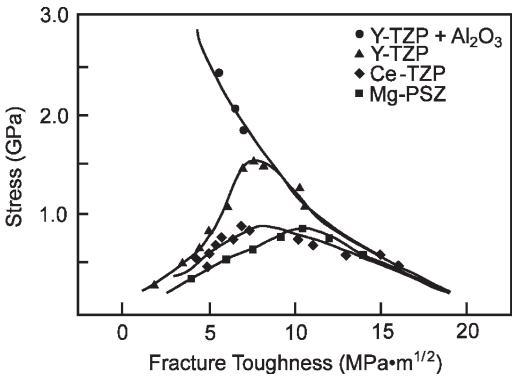

Fig. 10 Strength vs. fracture toughness for a selection of ZrO_2-toughened engineering ceramics [29] (reprinted with permission)

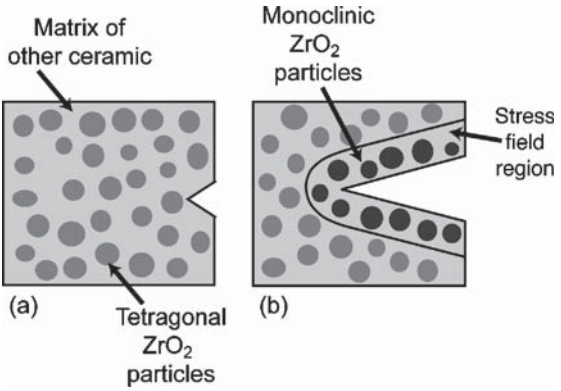

Fig. 11 Transformation toughening mechanism in a composite that contains small tetragonal zirconia particles

a stress (Fig. 11a). If the composite contains metastable tetragonal particles, the large stresses at the tip of the crack can force the tetragonal-to-monoclinic transformation of these particles increasing the volume of material in the region of the crack and forcing crack closure (Fig. 11b). The positive change in volume during the transformation is small but significant. If the positive change in volume is large, it can result in fragmentation of the material. On the other hand, a negative change in volume will not result in strains that promote crack closure. Hence, zirconia is quite unique in that the monoclinic and tetragonal structures are very close in density such that exaggerated volume increases are avoided during transformation. As the amount of dopant is increased, the stability of the tetragonal phase is higher and the transformation becomes more sluggish.

Indeed, Bravo-Leon et al. [31] and Sakuma et al. [34] have found that the toughness is higher for samples with yttria concentrations lower than the typical 3 mol% used for this material. Fracture toughness values of 16–17 MPa $m^{1/2}$ were reached by Bravo-Leon et al. for a 1 mol% yttria specimen with a grain size of 90 nm and a 1.5 mol% yttria specimen with a grain size of 110 nm. This can be attributed to the lower stability of the tetragonal phase with low dopant concentrations, which easily transforms to the monoclinic phase upon application of the stress.

4.4 Creep

Using the strain rate data shown in Fig. 12, the activation energy for creep in monoclinic zirconia has been found to be $Q_c \approx 330$–360 kJ mol^{-1} [48, 49]. The measured stress exponent, n, from equation:

$$\dot{\varepsilon} = A\frac{Gb}{kT}\left(\frac{b}{d}\right)^{p}\left(\frac{\sigma}{G}\right)^{n} D, \tag{3}$$

was found to be 1.7 by Roddy et al. [48] and 2.3–2.5 by Yoshida et al. [49]. In this equation, A is a constant, G is the shear modulus, b is the Burger's vector, d is the grain size,

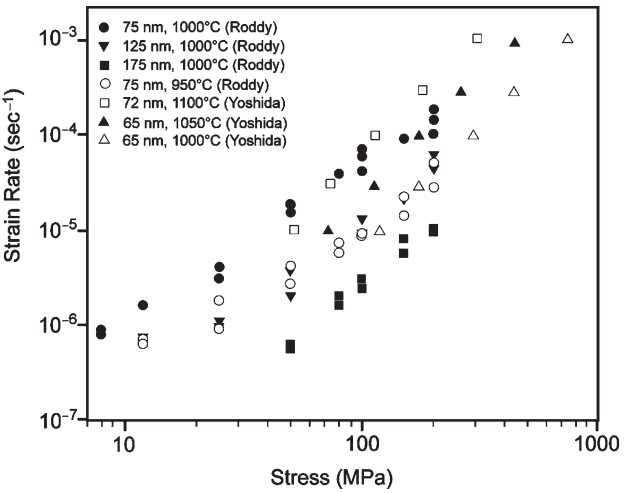

Fig. 12 Stress dependence of monoclinic zirconia during creep deformation (adapted from Roddy et al. [48] and Yoshida et al. [49])

σ is the applied stress, p is the grain size exponent, n is the stress exponent, and D is the diffusion coefficient. The value by Roddy et al. is intermediate between diffusional creep ($n = 1$) and superplastic deformation ($n = 2$), but closer to superplastic deformation, whereas the values by Yoshida et al. are higher than both, but close to the stress exponent for superplastic deformation. The grain size exponent, p, was found to be 2.8 by Roddy et al., which is closer to $p = 3$ for Coble creep (lattice diffusion) than $p = 2$ for superplastic or Nabarro-Herring creep (grain boundary diffusion). However, Yoshida et al. found values between 2.4 and 2.5. From the exponents found in both studies, it is likely that creep deformation in monoclinic zirconia is due to superplastic deformation.

5 Electronic Properties

Cubic zirconia doped with oxides such as Y_2O_3 or CaO is the material of choice for many high temperature applications because of its extremely high ionic conductivity at intermediate and high temperatures. A review on the properties of these specialized rare-earth stabilized zirconia materials has been prepared by Comins et al. [50].

The oxygen pressure dependence of the conductivity in tetragonal zirconia can be seen in Fig. 13 [51]. This material is a mixed electronic and ionic conductor with a large ionic contribution except at very high temperatures or very low oxygen partial pressures. The electronic component of the conductivity arises from doubly-charged oxygen vacancies at lower oxygen pressures and a temperature of 1,400°C. Other contributions to conductivity are difficult to determine. The movement of oxygen vacancies can take place along two directions for the tetragonal structure: within the x–y plane along the [110] direction or perpendicular to this plane along the [001] direction. In both directions, the O–O distances are very similar (0.2640 nm within the (x, y) plane and 0.2644 nm in the direction perpendicular to that plane) [25]. From these numbers, it would appear that there is no preferential direction for diffusion.

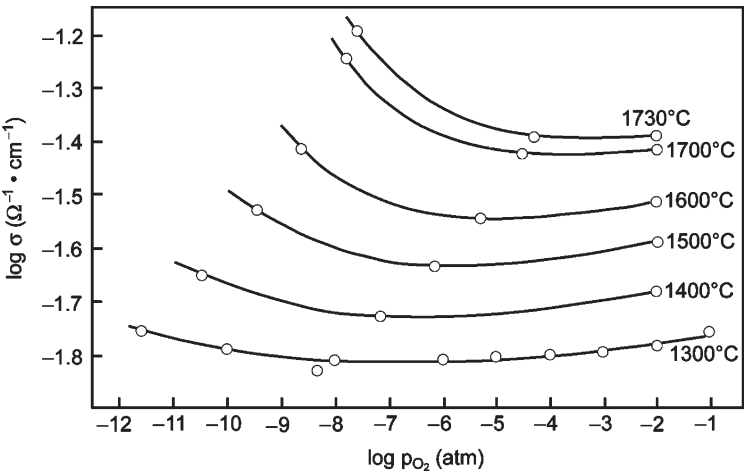

Fig. 13 Conductivity isotherms for tetragonal zirconia as a function of oxygen pressure [51] (reprinted with permission)

However, the diffusion process is controlled by the Zr–Zr distance and not by the O–O distance, since the vacancy must move between two such ions to diffuse. Along the two relevant directions, these distances are 0.3655 nm for the [110] direction and 0.3645 nm for the [001] direction. The diffusion barriers for movement of a neutral vacancy along [110] and [001] are 1.35 and 1.43 eV, respectively. This is expected from the fact that there is a smaller gap between zirconium ions along the [001] direction. Hence, diffusion along this direction proves to be more difficult. The diffusion barriers for movement of a doubly-charged vacancy along the two relevant directions are 0.22 and 0.61 eV, respectively. Again, movement along the [001] direction proves to be more difficult. This can be visualized in Fig. 14 [6].

Monoclinic zirconia is both an electron and ion conductor depending on the temperature and oxygen pressure (Fig. 15) [52–54]. At low pressures, it exhibits n-type behavior in which the charge carriers are double-charged oxygen vacancies, while at higher pressures it exhibits p-type behavior in which the charge carriers are singly-ionized oxygen interstitials. The transition from n-type to p-type is established by the change in sign of the conductivity curve. Assuming the -1/6 and 1/5 dependences in the two regions are good fits to the data, the total conductivity at 1,000°C can be represented by:

$$\sigma_{1,000^\circ C} \cong 8.5\times10^{-5}\ p_{O_2}{}^{1/5} + 1.1\times10^{-9}\ p_{O_2}{}^{-1/6} + 3.2\times10^{-6}. \qquad (4)$$

In addition, Vest et al. [53] determined the hole mobility at 1,000°C to be $\mu_{1,000^\circ C} = 1.4\times10^{-6}\ cm^2 \bullet V^{-1} \bullet s^{-1}$.

If the pressure is kept constant and the temperature is increased, the conductivity also increases (see Fig. 4 of Kumar et al. [52]). At lower temperatures (< 600°C), conductivity is predominantly ionic, and at higher temperatures (> 700°C), it is predominately electronic. Between 600 and 700°C, both ionic and electronic conductivities are seen in this material. Values of the activation energies required for each type of

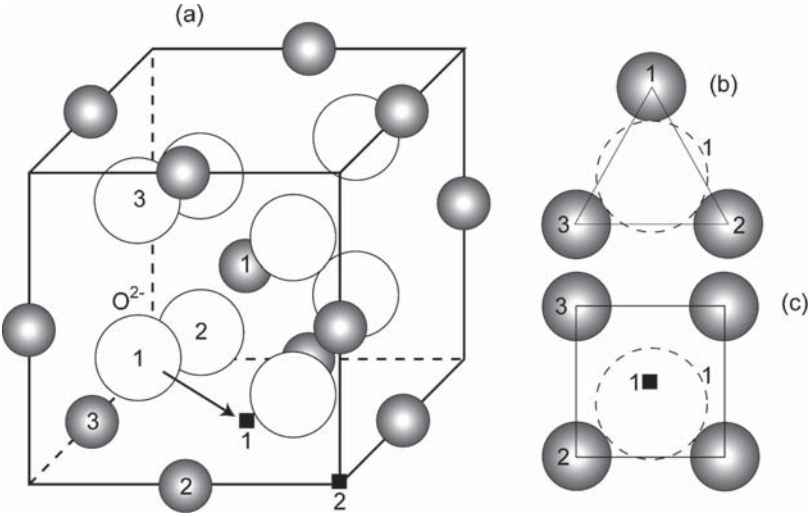

Fig. 14 Simplified representation of possible diffusion mechanism for oxygen atoms in tetragonal zirconia. (**a**) Tetragonal cell with two octahedral empty sites, marked with *black squares* 1 and 2, (**b**) Position of oxygen 1 during its motion past the zirconium 1–3 face, (**c**) possible off-centered position for oxygen 1 inside octahedral site 1 (adapted from [6])

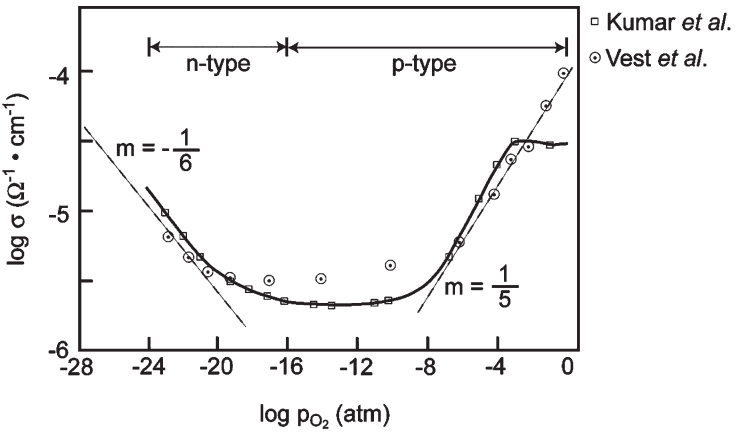

Fig. 15 Oxygen pressure dependence of total conductivity for monoclinic zirconia at 990°C (adapted from Kumar et al. [52] and Vest et al. [53])

conductivity are still a matter of controversy because of the complexity of the conduction processes. Earlier values include numbers such as 3.56 eV for n-type conductivity and 0.86 eV for p-type conductivity [55].

The conductivity of two high-pressure phases of zirconia is shown in Fig. 16 [56]. The discontinuities in the conductivity occur approximately at 1,000°C for the sample at 16.5 GPa and 1,050°C for the sample at 18.0 GPa. At the higher temperatures, the conductivity corresponds to a so-called "cubic" high-pressure and high-temperature phase of zirconia, although its exact nature was not determined by Ohtaka et al. [56].

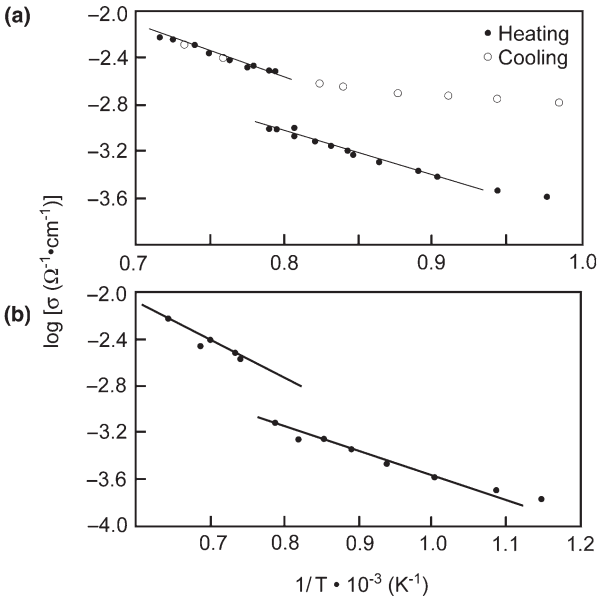

Fig. 16 Electrical conductivity of pure cubic zirconia at (a) 16.5 GPa and (b) 18 GPa [56] (reprinted with permission)

At the lower temperatures, the conductivity corresponds to the orthorhombic-II phase. From the Arrhenius plots in the figure, approximate activation energies for conduction can be obtained. For the "cubic" phase, the activation energies are 8.80 and 0.60 eV at pressures of 16.5 and 18.0 GPa, respectively, while for the orthorhombic-II phase they are 0.72 and 0.40 eV for the two pressures studied.

6 Diffusion Coefficients

Diffusion in zirconia is closely linked to ionic conductivity. Consequently, some diffusion data has already been presented in Sect. 5. This section will include additional results particularly for monoclinic zirconia. Oxygen self-diffusion at a pressure of 300 Torr, as determined by testing zirconia spheres of diameters between 75 and 105 μm, behaves as shown in Fig. 17 [57], where D is the diffusion coefficient, t is time, and a is the sphere radius. At a pressure of 700 Torr, the behavior changes to that shown in Fig. 18 [58]. In this case D^* is the self-diffusion coefficient and the rest of the terms are as defined before, with a = 100–150 μm. Both of these experiments were performed in an oxygen atmosphere of ^{18}O–^{16}O. The self-diffusion coefficients calculated from the diffusion data obey Arrhenius expressions as illustrated in Fig. 19 [57, 58]. The linear fits describing the diffusion coefficient at 300 and 700 Torr, are given by:

$$P = 300\ \text{Torr} : D\left(\frac{\text{cm}^2}{s}\right) = 9.73 \pm 1.4 \times 10^{-3} \exp\left\{-\frac{56.0 \pm 2.4\ \text{kcal/mol}}{RT}\right\} \qquad (5)$$

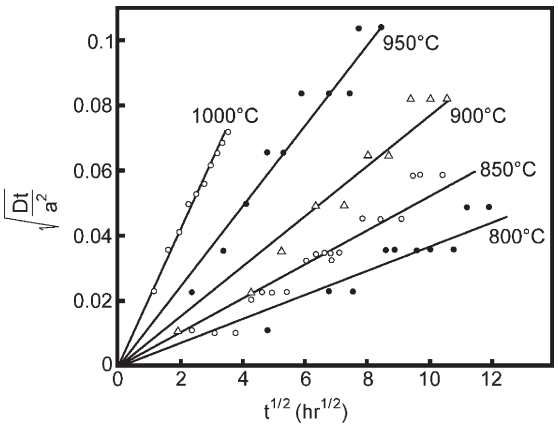

Fig. 17 Oxygen diffusion in monoclinic zirconia spheres at 300 Torr [57] (reprinted with permission)

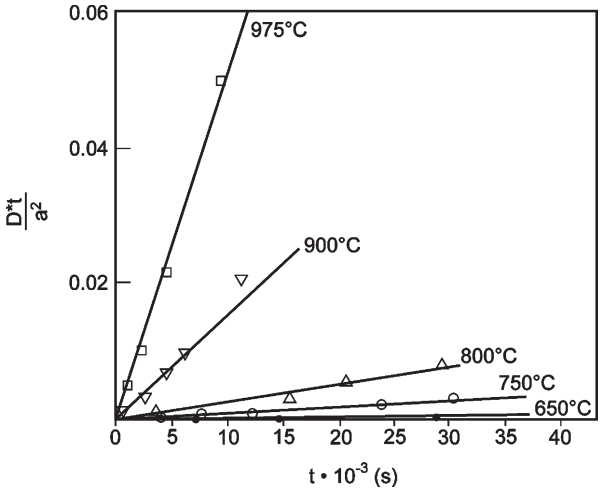

Fig. 18 Oxygen diffusion in monoclinic zirconia spheres at 700 Torr [58] (reprinted with permission)

$$P = 700 \text{ Torr: } D\left(\frac{\text{cm}^2}{s}\right) = 2.34\times10^{-2}\exp\left\{-\frac{45300\pm1200 \text{ cal/mol}}{RT}\right\}. \tag{6}$$

According to Ikuma et al. [59], surface diffusion and lattice diffusion should be separated and result in the following diffusion coefficients:

$$D_{surface}\left(\text{cm}^2/s\right) = 5.84\times10^{-12}\exp\left\{-\frac{75.3 \text{ kJ/mol}}{RT}\right\} \tag{7}$$

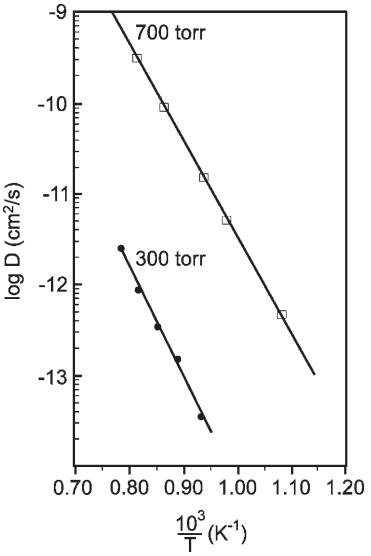

Fig. 19 Arrhenius plot of oxygen self-diffusion in monoclinic zirconia (adapted from Madeyski and Smeltzer [57] and Keneshea and Douglass [58])

$$D_{lattice}\left(\mathrm{cm}^2/s\right) = 4.84\times10^{-12}\exp\left\{-\frac{87.0\ \mathrm{kJ/mol}}{RT}\right\}. \tag{8}$$

These two expressions are not that very different. Hence, the macroscopic diffusion behavior of monoclinic zirconia can be approximated by lattice diffusion, while surface diffusion can be ignored.

Diffusion in pure tetragonal and cubic zirconia is experimentally challenging because it requires the higher temperatures at which the two phases are stable. However, simulations at temperatures between 1,273 and 2,673 K have been performed on cubic zirconia, showing noticeable, but not large, oxygen ion diffusion along the grain boundaries and a significant energy barrier to movement from the grain boundaries into the bulk, although at higher temperatures diffusion is obviously enhanced. However, even at higher temperatures, diffusion along the grain boundary is not as favorable as that across the grain boundary [60].

7 Phase Transitions and the Processing of Zirconia

Upon heating, the monoclinic phase in zirconia starts transforming to the tetragonal phase at 1,461 K, peaks at 1,471 K, and finishes at 1,480 K. On cooling, the transformation from the tetragonal to the monoclinic phase starts at 1,326 K, peaks at 1,322 K, and finishes at 1,294 K, exhibiting a hysteresis behavior that is well known for this material [61–65]. This transformation can also be affected by irradiation with heavy ions, such as 300 MeV Ge [66] and 340 keV Xe [67].

The tetragonal phase transforms to the cubic fluorite structure at 2584 ± 15 K [68]. This transformation temperature has been found to be dependent on the atmosphere

in which the transformation is taking place [6]. In a reducing atmosphere, the transformation takes place at approximately 2,323 K, and in a neutral atmosphere, it takes place at approximately 2,563 K, which is in proximity to the highly accurate value found by Navrotsky et al. [68]. Continued heating of the material results in melting at a temperature of 2,963 K [63]. The phase stability as a function of pressure for this material in its pure form is shown in Fig. 20 [7].

The practical use of pure zirconia is restricted by the monoclinic to tetragonal transformation, as this transformation causes cracking and sometimes complete disintegration of the specimen. Depending on the orientation of the particular grain that is undergoing the transformation, there is a maximum strain in the lattice of ~4% [29], which is quite significant and promotes failure of the specimen when undergoing heating and cooling cycles.

This transformation has many characteristics of martensitic transformations in metals, with definite orientation relationships between the two structures. The orientation relationships conform to the following [69–71]:

$$\left.\begin{array}{l}(100)_{\mathrm{m}} \| (110)_{\mathrm{bct}} \text{ and } [010]_{\mathrm{m}} \| [001]_{\mathrm{bct}}, \\ \text{and by twinning } (100)_{\mathrm{m}} \| (110)_{\mathrm{bct}} \text{ and } [001]_{\mathrm{m}} \| [001]_{\mathrm{bct}}\end{array}\right\} \tag{9}$$

where m and t represent the monoclinic and tetragonal phases, and bct refers to the body-centered tetragonal structure. Possible variants of these twin relationships for small tetragonal particles are shown in Fig. 21. In this figure, the hashed areas represent the transformed monoclinic phase and the unhashed areas represent the

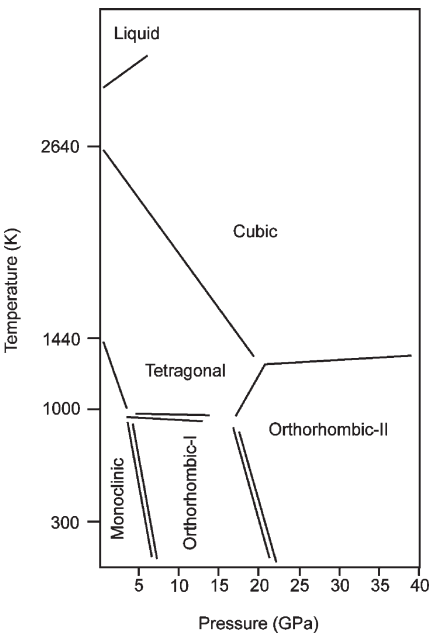

Fig. 20 Pressure–temperature phase diagram of zirconia [7] (reprinted with permission)

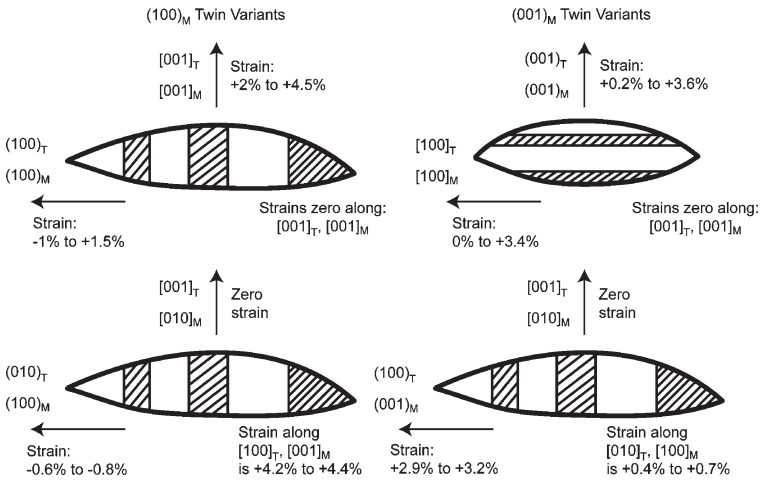

Fig. 21 The four possible arrangements of twin-related variants together with the range of strain values predicted for the directions indicated (adapted from Kelly [76])

untransformed tetragonal phase. As the transformation progresses, the entire particle eventually forms the stable monoclinic phase for this material. The transformation progresses in two stages. The first stage involves a displacive transformation with small shifts of the atoms and the second stage involves a martensitic transformation in which both structures remain almost unchanged [72]. It is this latter transformation that has been studied the most thoroughly [73–75].

To avoid this destructive transformation, stabilization of the tetragonal and cubic structures of zirconia can be done at room temperature by the addition of trivalent dopant ions such as Y^{3+} and Ce^{3+}, divalent dopant ions such as Ca^{2+}, or tetravalent dopant ions. Doping of zirconia has enormous consequences not only for the mechanical properties of this material, but also for the electronic properties. In particular, Y^{3+} has a large solubility range in zirconia and can be used to stabilize both the tetragonal and cubic phases. To maintain charge neutrality, one oxygen vacancy must be created for each pair of dopant cations that are added to the structure. This results in large increases in ionic conductivity. Stabilization of the tetragonal and cubic structures requires differing amounts of dopants. The tetragonal phase is stabilized at lower dopant concentrations. The cubic phase is stabilized at higher dopant concentrations, as shown in the room temperature region of the ZrO_2–Y_2O_3 phase diagram in Fig. 22 [77]. At higher Y_2O_3 doping, the material exhibits an ordered $Zr_3Y_4O_{12}$ phase at 40 mol% Y_2O_3, a eutectoid at a temperature $<400°C$ at a composition between 20 and 30 mol% Y_2O_3, a eutectic at 83 ± 1 mol% Y_2O_3, and a peritectic at 76 ± 1 mol% Y_2O_3 [78]. Other zirconia phase diagrams have been developed by Stubican and Ray for ZrO_2–CaO [79], Grain for ZrO_2–MgO [80], Cohen and Schaner for ZrO_2–UO_2 [81], Mumpton and Roy for ZrO_2–ThO_2 [82], Barker et al [83] for ZrO_2–Sc_2O_3, and Duwez and Odell for ZrO_2–CeO_2 [84], among others.

As mentioned briefly in Sect. 4, another way of stabilizing the tetragonal structure at room temperature is the formation of nanocrystalline powders or nanograined sintered specimens. To obtain powders of dense PSZ compacts at room temperature, the material has to contain crystals or grains below a certain critical size, which

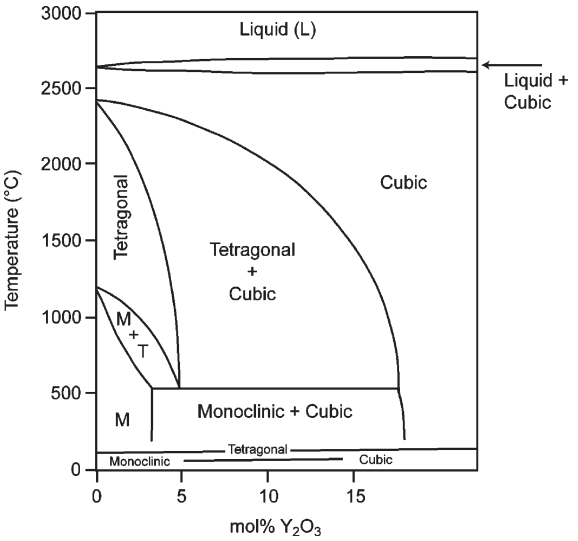

Fig. 22 Zirconia-rich end of the yttria-zirconia phase equilibrium diagram [77] (reprinted with permission)

increases as the dopant concentration increases. The critical size is 22.6 (also found to be ~18 nm by Chraska et al. [85] and 15.3 nm by Garvie [86]), 41.7, 67, and 93.8 nm for yttria doping concentrations of 0, 0.5, 1.0, and 1.5 mol% [87]. The values decrease with increasing dopant concentration, consistent with the fact that yttria is a tetragonal-phase stabilizer. Changes in the transformation temperature with dopant concentration and crystallite size are shown in Fig. 23 [87], where it can be seen that the transformation temperature decreases with decreasing crystallite size and increasing dopant concentration. The dotted lines represent theoretical curves calculated according to:

$$T_{\text{transformation}} = \frac{\Delta H_{\text{vol}} + \dfrac{10\Delta h_{\text{surf}}}{d_{\text{critical}}}}{\Delta S_{\text{vol}} + \dfrac{10\Delta s_{\text{surf}}}{d_{\text{critical}}}}, \tag{10}$$

where ΔH_{vol} is the volumetric heat of transformation, Δh_{surf} is the surface enthalpy difference, d_{critical} is the critical crystallite size to stabilize the tetragonal phase at room temperature, ΔS_{vol} is the volumetric entropy of transformation, and Δs_{surf} is the surface entropy difference. The solid curves are from the standard ZrO_2–Y_2O_3 phase diagram (Fig. 22). The solid circles represent experimental data on samples that happened to have crystallite sizes close to those for which the theoretical curves were calculated.

The stabilization of the tetragonal phase at room temperature due to a decrease in the crystallite size has been attributed to a surface energy difference and roughly obeys the relationships [88]:

$$\frac{1}{d_{\text{critical}}} = -\frac{\Delta H_{\infty} T}{6\Delta\gamma T_b} + \frac{\Delta H_{\infty}}{6\Delta\gamma} \text{ (for powders)} \tag{11}$$

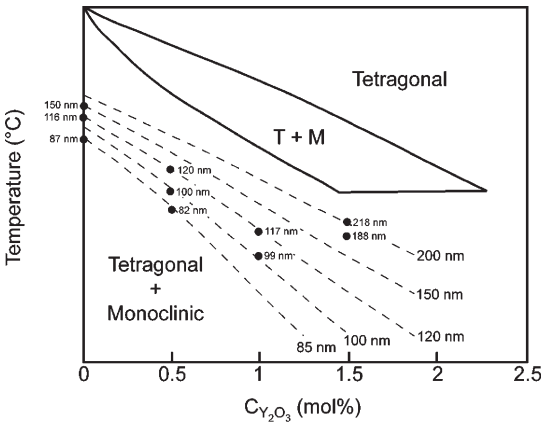

Fig. 23 Phase diagram representation of the crystallite size and yttria concentration dependency of the tetragonal-to-monoclinic transformation temperature [87] (reprinted with permission)

$$\frac{1}{d_{critical}} = -\frac{\Delta H_{\infty} T}{6\Delta\Sigma T_b} + \frac{\Delta H_{\infty} + \Delta U_{se}}{6\Delta\Sigma} \text{ (for sintered pellets)} \tag{12}$$

where $d_{critical}$ is the critical crystallite/grain size, ΔH_{∞} is the enthalpy of the tetragonal-to-monoclinic phase transformation in a sample with infinite crystallite/grain size, T is the temperature of transformation, $\Delta\gamma$ is the difference in surface energy in powder crystallites, $\Delta\Sigma$ is the difference in interfacial energy in sintered pellets, T_b is the transformation temperature for an infinitely large-grained sample, and ΔU_{se} is the strain energy involved in the transformation. From these equations, it can be seen that the same material in the solid form has a lower transformation temperature than in the powder form. This difference is due to the strain energy, ΔU_{se}, involved in the transformation, which is present only in the pellets since there is a requirement for geometric compatibility that is not present in the powders.

References

1. G. Stapper, M. Bernasconi, N. Nicoloso, and M. Parrinello, Ab initio study of structural and electronic properties of yttria-stabilized cubic zirconia, *Phys. Rev. B*, **59**(2), 797–810 (1999).
2. J.K. Dewhurst and J.E. Lowther, Relative stability, structure, and elastic properties of several phases of pure zirconia, *Phys. Rev. B*, **57**(2), 741–747 (1998).
3. P. Li, I.-W. Chen, and J.E. Penner-Hahn, Effect of dopants on zirconia stabilization – An X-ray absorption study: I, trivalent dopants, *J. Am. Ceram. Soc.* **77**(1) 118–128 (1994).
4. D.W. Richerson, *Modern Ceramic Engineering Properties, Processing, and Use in Design 3/e*, Taylor and Francis Group, Boca Raton, 2006, p 30.
5. S.-M. Ho, On the structural chemistry of zirconium oxide, *Mater. Sci. Eng.* **54**, 23–29 (1982).

6. P. Aldebert and J.-P. Traverse, Structure and ionic mobility of zirconia at high temperature, *J. Am. Ceram. Soc.* **68**(1), 34–40 (1985).
7. P. Bouvier, E. Djurado, G. Lucazeau, and T. Le Bihan, High-pressure structural evolution of undoped tetragonal nanocrystalline zirconia, Phys. Rev. B **62**(13), 8731–8737 (2000).
8. N. Igawa and Y. Ishii, Crystal structure of metastable tetragonal zirconia up to 1473 K, J. Am. Ceram. Soc. **84**(5), 1169–1171 (2001).
9. G. Teufer, The crystal structure of tetragonal ZrO_2, *Acta Crystallogr.* **15**, 1187 (1962).
10. M. Winterer, Reverse Monte Carlo analysis of extended x-ray absorption fine structure spectra of monoclinic and amorphous zirconia, *J. Appl. Phys.* **88**(10), 5635–5644 (2000).
11. P. Li, I.-W. Chen, and J.E. Penner-Hahn, X-ray-absorption studies of zirconia polymorphs. I. Characteristic local structures, Phys. Rev. B, **48**(14), 10063–10073 (1993).
12. J.D. McCullough and K.N. Trueblood, The crystal structure of baddeleyite (monoclinic ZrO2), *Acta Crystallogr.* **12**, 507–511 (1959)
13. H. Arashi, T. Suzuki, ad S.-I. Akimoto, Non-destructive phase transformation of ZrO_2 single crystal at high pressure, *J. Mater. Sci. Lett.* **6**, 106–108 (1987).
14. S. Kawasaki, T. Yamanaka, S. Kume, and T. Ashida, Crystallite size effect on the pressure-induced phase transformation of ZrO_2, *Solid State Commun.* **76**(4), 527–530 (1990).
15. S. Desgreniers and K. Lagarec, High-density ZrO_2 and HfO_2: Crystalline structures and equations of state, *Phys. Rev. B*, **59**(13), 8467–8472 (1999).
16. C.J. Howard, E.H. Kisi, and O. Ohtaka, Crystal structures of two orthorhombic zirconias, *J. Am. Ceram. Soc.* **74**(9), 2321–2323 (1991).
17. E.H. Kisi, C.J. Howard, and R.J. Hill, Crystal structure of orthorhombic zirconia in partially stabilized zirconia, *J. Am. Ceram. Soc.* **72**(9), 1757–1760 (1989).
18. O. Ohtaka, T. Yamanaka, and T. Yagi, New high-pressure and –temperature phase of ZrO_2 above 1000°C at 20 GPa, *Phys. Rev. B*, **49**(14), 9295–9298 (1994).
19. J. Livage, K. Doi, and C. Mazieres, Hydrated zirconium oxide, *J. Am. Ceram. Soc.* **51**(6), 349–353 (1968).
20. A. Clearfield, Crystalline hydrous zirconia, *Inorg. Chem.* **3**(1), 146–148 (1964).
21. C. Landron, A. Douy, and D. Bazin, From liquid to solid: residual disorder in the local environment of oxygen-coordinated zirconium, *Phys. Status Solidi B*, **184**, 299–307 (1994).
22. A. Corina Geiculescu and H.J. Rack, Atomic-scale structure of water-based zirconia xerogels by X-ray diffraction, *J. Sol–Gel Sci. Technol.* **20**, 13–26 (2001).
23. A.V. Chadwick, G. Mountjoy, V.M. Nield, I.J.F. Poplett, M.E. Smith, J.H. Strange, and M.G. Tucker, Solid-state NMR and X-ray studies of the structural evolution of nanocrystalline zirconia, *Chem. Mater.* **13**, 1219–1229 (2001).
24. A.S. Foster, V.B. Sulimov, F. Lopez Gejo, A.L. Shluger, and R.M. Nieminen, Structure and electrical levels of point defects in monoclinic zirconia, *Phys. Rev. B*, **64**, 224108 (2001).
25. A. Eichler, Tetragonal Y-doped zirconia: structure and ion conductivity, *Phys. Rev. B*, **64**, 174103 (2001).
26. R.W. Vest, N.M. Tallan, and W.C. Tripp, Electrical properties and defect structure of zirconia: I, monoclinic phase, *J. Am. Ceram. Soc.* **47**(12), 635–640 (1964).
27. A.H. Heuer, Transformation toughening in ZrO_2-containing ceramics, *J. Am. Ceram. Soc.* **70**(10), 689–698 (1987).
28. U. Messerschmidt, B. Baufeld, and D. Baither, Plastic deformation of cubic zirconia single crystals, *Key Eng. Mater.* **153–154**, 143–182 (1998).
29. R.H.J. Hannink, P.M. Kelly, and B.C. Muddle, Transformation toughening in zirconia-containing ceramics, *J. Am. Ceram. Soc.* **83**(3), 461–487 (2000).
30. S.-K. Chan, Y. Fang, M. Grimsditch, Z. Li, M.V. Nevitt, W.M. Robertson, and E.S. Zouboulis, Temperature dependence of the elastic moduli of monoclinic zirconia, *J. Am. Ceram. Soc.* **74**(7), 1742–1744 (1991).
31. A. Bravo-Leon, Y. Morikawa, M. Kawahara, and M.J. Mayo, Fracture toughness of nanocrystalline tetragonal zirconia with low yttria content, *Acta Mater.* **50**, 4555–4562 (2002).
32. R.A. Cutler, J.R. Reynolds, and A. Jones, Sintering and characterization of polycrystalline monoclinic, tetragonal, and cubic zirconia, *J. Am. Ceram. Soc.* **75**(8), 2173–2183 (1992).

33. M. Levichkova, V. Mankov, N. Starbov, D. Karashanova, B. Mednikarov, and K. Starbova, Structure and properties of nanosized electron beam deposited zirconia thin films, *Surf. Coat. Technol.* **141**, 70–77 (2001).
34. T. Sakuma, Y.-I. Yoshizawa, and H. Suto, The microstructure and mechanical properties of yttria-stabilized zirconia prepared by arc-melting, *J. Mater. Sci.* **20**, 2399–2407 (1985).
35. G. Skandan, H. Hahn, M. Roddy, and W.R. Cannon, Ultrafine-grained dense monoclinic and tetragonal zirconia, *J. Am. Ceram. Soc.* **77**(7), 1706–1710 (1994).
36. J. Eichler, U. Eisele, and J. Rödel, Mechanical properties of monoclinic zirconia, *J. Am. Ceram. Soc.* **87**(7), 1401–1403 (2004).
37. Y.-M. Chiang, D. Birnie III, and W.D. Kingery, *Physical Ceramics Principles for Ceramic Science and Engineering*, Wiley, New York, 1997, p. 484.
38. D.W. Richerson, *Modern Ceramic Engineering Properties, Processing, and Use in Design 3/e* Taylor and Francis Group, Boca Raton, 2006, pp. 275, 643.
39. G. Stefanic and S. Music, Factors influencing the stability of low temperature tetragonal ZrO_2, *Croat. Chem. Acta* **75**(3), 727–767 (2002).
40. H.S. Maiti, K.V.G.K. Gokhale, and E.C. Subbarao, Kinetics and burst phenomenon in ZrO_2 transformation, *J. Am. Ceram. Soc.* **55**(6), 317–322 (1972).
41. A.H. Heuer, N. Claussen, W.M. Kriven, and M. Rühle, Stability of tetragonal ZrO_2 particles in ceramic matrices, *J. Am. Ceram. Soc.* **65**(12), 642–650 (1982).
42. M.H. Bocanegra-Bernal and S. Diaz De La Torre, Review. Phase transitions in zirconium dioxide and related materials for high performance engineering materials, *J. Mater. Sci.* **37**, 4947–4971 (2002).
43. A.G. Evans, N. Burlingame, M. Drory, and W.M. Kriven, Martensitic transformations in zirconia–particle size effects and toughnening, *Acta Metall.* **29**, 447–456 (1981).
44. A.G. Evans and A.H. Heuer, Review – Transformation toughening in ceramics: Martensitic transformations in crack-tip stress fields, *J. Am. Ceram. Soc.* **63**(5–6), 241–248 (1980).
45. D.W. Richerson, *Modern Ceramic Engineering Properties, Processing, and Use in Design* Taylor and Francis Group, Boca Raton, 2006, pp. 635, 640–644.
46. T.K. Gupta, F.F. Lange, and J.H. Bechtold, Effect of stress-induced phase transformation on the properties of polycrystalline zirconia containing metastable tetragonal phase, *J. Mater. Sci.* **13**(7), 1464–1470 (1978).
47. Y.-M. Chiang, D. Birnie III, and W.D. Kingery, *Physical Ceramics Principles for Ceramic Science and Engineering*, Wiley, New York, 1997, pp. 488–492.
48. M.J. Roddy, W.R. Cannon, G. Skandan, and H. Hahn, Creep behavior of nanocrystalline monoclinic ZrO_2, *J. Eur. Ceram. Soc.* **22**, 2657–2662 (2002).
49. M. Yoshida, Y. Shinoda, T. Akatsu, and F. Wakai, Superplasticity-like deformation of nanocrystalline monoclinic zirconia at elevated temperatures, *J. Am. Ceram. Soc.* **87**(6), 1122–1125 (2004).
50. J.D. Comins, P.E. Ngoepe, and C.R.A. Catlow, Brillouin-scattering and computer-simulation studies of fast-ion conductors. A review, *J. Chem. Soc. Faraday Trans.* **86**(8), 1183–1192 (1990).
51. R.W. Vest and N.M. Tallan, Electrical properties and defect structure of zirconia: II, tetragonal phase and inversion, *J. Am. Ceram. Soc.* **48**(9), 472–475 (1965).
52. A. Kumar, D. Rajdev, and D.L. Douglass, Effect of oxide defect structure on the electrical properties of ZrO_2, *J. Am. Ceram. Soc.* **55**(9), 439–445 (1972).
53. R.W. Vest, N.M. Tallan, and W.C. Tripp, Electrical properties and defect structure of zirconia: I, monoclinic phase, *J. Am. Ceram. Soc.* **47**(12), 635–640 (1964).
54. P. Kofstad and D.J. Ruzicka, On the defect structure of ZrO_2 and HfO_2, *J. Electrochem. Soc.* **110**(3), 181–184 (1963).
55. E. Dow Whitney, Electrical resistivity and diffusionless phase transformation of zirconia at high temperatures and ultrahigh pressures, *J. Electrochem. Soc.* **112**(1), 91–94 (1965).
56. O. Ohtaka, S. Kume, and E. Ito, Stability field of cotunnite-type zirconia, *J. Am. Ceram. Soc.* **73**(3), 744–745 (1990).
57. A. Madeyski and W.W. Smeltzer, Oxygen diffusion in monoclinic zirconia, *Mater. Res. Bull.* **3**, 369–376 (1968).

58. F.J. Keneshea and D.L. Douglas, The diffusion of oxygen in zirconia as a function of oxygen pressure, *Oxidation Met.* **3**(1), 1–14 (1971).
59. Y. Ikuma, K. Komatsu, and W. Komatsu, Oxygen diffusion in monoclinic ZrO_2, undoped and doped with Y_2O_3, *Adv. Ceram.* **24**, 749–758 (1988).
60. C.A.J. Fisher and H. Matsubara, Molecular dynamics investigations of grain boundary phenomena in cubic zirconia, *Comput. Mater. Sci.* **14**, 177–184 (1999).
61. Y. Moriya and A. Navrotsky, High-temperature calorimetry of zirconia: heat capacity and thermodynamics of the monoclinic-tetragonal phase transition, *J. Chem. Thermodyn.* **38**, 211–223 (2006).
62. H. Boysen, F. Frey, and T. Vogt, Neutron powder investigation of the tetragonal to monoclinic phase transformation in undoped zirconia, *Acta Crystallogr. B*, **47**, 881–886 (1991).
63. R. Ruh, H.J. Garrett, R.F. Domagala, and N.M. Tallan, The system zirconia-hafnia, *J. Am. Ceram. Soc.* **51**(1), 23–27 (1968).
64. G.M. Wolten, Diffusionless phase transformations in zirconia and hafnia, *J. Am. Ceram. Soc.* **46**(9), 418–422 (1963).
65. W.L. Baun, Phase transformation at high temperatures in hafnia and zirconia, *Science*, **140**(3573), 1330–1331 (1963).
66. A. Benyagoub, F. Levesque, F. Couvreur, C. Gibert-Mougel, C. Dufour, and E. Paumier, Evidence of a phase transition induced in zirconia by high energy heavy ions, *Appl. Phys. Lett.* **77**(20), 3197–3199 (2000).
67. K.E. Sickafus, H. Matzke, T. Hartmann, K. Yasuda, J.A. Valdez, P. Chodak III, M. Nastasi, and R.A. Verrall, Radiation damage effects in zirconia, *J. Nucl. Mater.* **274**, 66–77 (1999).
68. A. Navrotsky, L. Benoist, and H. Lefebvre, Direct calorimetric measurement of enthalpies of phase transitions at 2000–2400°C in yttria and zirconia, *J. Am. Ceram. Soc.* **88**(10), 2942–2944 (2005).
69. J.E. Bailey, The monoclinic-tetragonal transformation and associated twinning in thin films of zirconia, *Proc. Roy. Soc. Lon. Ser. A, Math. Phys. Sci.* **279**(1378), 395–412 (1964).
70. S.T. Buljan, H.A. McKinstry, and V.S. Stubican, Optical and X-ray single crystal studies of the monoclinic tetragonal transition in ZrO_2, *J. Am. Ceram. Soc.* **59**(7–8), 351–354 (1976).
71. R.N. Patil and E.C. Subbarao, Monoclinic-tetragonal phase transition in zirconia: Mechanism, pretransformation and coexistence, *Acta Crystallogr. A* **26**, 535–542 (1970).
72. F. Frey, H. Boysen, and T. Vogt, Neutron powder investigation of the monoclinic to tetragonal phase transformation in undoped zirconia, *Acta Crystallogr. B* **46**, 724–730 (1990).
73. E.C. Subbarao, H.S. Maiti, and K.K. Srivastava, Martensitic transformation in zirconia, *Phys. Status Solidi A* **21**, 9–40 (1974).
74. G.K. Bansal and A.H. Heuer, On a martensitic phase transformation in zirconia (ZrO_2)-I. Metallographic evidence, *Acta Metall.* **20**, 1281–1289 (1972).
75. G.K. Bansal and A.H. Heuer, On a martensitic phase transformation in zirconia (ZrO_2)-II. Crystallographic aspects, *Acta Metall.* **22**, 409–417 (1974).
76. P.M. Kelly, Martensitic transformations in ceramics, *Mater. Sci. Forum*, **56–58**, 335–346 (1990).
77. D. Huang, K.R. Venkatachari, and G.C. Stangle, Influence of yttria content on the preparation of nanocrystalline yttria-doped zirconia, *J. Mater. Res.* **10**(3), 762–773 (1995).
78. V.S. Stubican, R.C. Hink, and S.P. Ray, Phase equilibria and ordering in the system ZrO_2–Y_2O_3, *J. Am. Ceram. Soc.* **61**(1–2), 17–21 (1978).
79. V.S. Stubican and S.P. Ray, Phase equilibria and ordering in the system ZrO_2–CaO, *J. Am. Ceram. Soc.* **60**(11–12), 534–537 (1977).
80. C.F. Grain, Phase relations in the ZrO_2–MgO system, *J. Am. Ceram. Soc.* **50**(6), 288–290 (1967).
81. I. Cohen and B.E. Schaner, A metallographic and x-ray study of the UO_2–ZrO_2 system, *J. Nucl. Mater.* **9**(1), 18–52 (1963).
82. F.A. Mumpton and R. Roy, Low-temperature equilibria among ZrO_2, ThO_2, and UO_2, *J. Am. Ceram. Soc.* **43**, 234–240 (1960).
83. W.W. Barker, F.P. Bailey, and W. Garrett, A high-temperature neutron diffraction study of pure and scandia-stabilized zirconia, *J. Solid State Chem.* **7**, 448–453 (1973).
84. P. Duwez and F. Odell, Phase relationships in the system zirconia-ceria, *J. Am. Ceram. Soc.* **33**(9), 274–283 (1950).
85. T. Chraska, A.H. King, and C.C. Berndt, On the size-dependent phase transformation in nanoparticulate zirconia, *Mater. Sci. Eng. A* **286**, 169–178 (2000).

86. R.C. Garvie, Stabilization of the tetragonal structure in zirconia microcrystals, *J. Phys. Chem.* **82**(2), 218–224 (1978).
87. A. Suresh, M.J. Mayo, and W.D. Porter, Thermodynamics of the tetragonal-to-monoclinic phase transformation in fine and nanocrystalline yttria-stabilized zirconia powders, *J. Mater. Res.* **18**(12), 2912–2921 (2003).
88. A. Suresh, M.J. Mayo, W.D. Porter, and C.J. Rawn, Crystallite and grain-size-dependent phase transformations in yttria-doped zirconia, *J. Am. Ceram. Soc.* **86**(2), 360–362 (2003).

Index